JGR Oceans

Key Points:

- Two different ocean eddy tracking algorithms are used to study the characteristics of coherent anticyclones in the Iceland Basin
- The number of anticyclones in the Iceland Basin covaries with decadal variability of ocean heat content in the Subpolar North Atlantic
- Increased anticyclonic activity in the Iceland Basin is linked to a westward shift in the subpolar front and enhanced subtropical advection

Supporting Information:

Supporting Information may be found in the online version of this article.

Correspondence to:

A. Kondetharayil Soman,
arunraj.kondetharayil@misu.su.se

Linking Coherent Anticyclonic Eddies in the Iceland Basin to Decadal Oceanic Variability in the Subpolar North Atlantic

Arunraj Kondetharayil Soman[1] [ID]**, Léon Chafik[1,2]** [ID]**, and Johan Nilsson[1]** [ID]

[1]Department of Meteorology and Bolin Centre for Climate Research, Stockholm University, Stockholm, Sweden, [2]National Oceanography Centre, Southampton, UK

Abstract The Iceland Basin in the eastern Subpolar North Atlantic is an eddy-rich region characterized by intense anticyclonic eddy activity. Our study present the variability of coherent Anticyclonic Eddies (AEs) generated in this region, using satellite altimetry and two ocean eddy tracking algorithms. The yearly count of AEs in the Iceland Basin reveals a decadal variability similar to that of ocean heat content change in the eastern subpolar gyre. Periods with higher number of AEs coincide with periods of increased ocean heat content, and vice versa. However, both algorithms agree that more than 50% of the detected AEs are confined to the central Iceland Basin. The annual number of AEs also tracks zonal shifts of the subpolar front, a variable that can explain about 53 (77)% of the interannual (decadal) variability of AEs in the Iceland Basin. Finally, a Lagrangian approach is used to demonstrate that the amount of subtropical versus subpolar water masses reaching the Iceland Basin appears to influence, via baroclinic instability, the generation of AEs.

Plain Language Summary The Iceland Basin in the Subpolar North Atlantic is a region of intense activity of swirling features. One of the reasons has to do with the flow of the Gulf Stream extension, the North Atlantic Current. This current does not only bring heat from lower latitudes into this basin but also tracks the front between cold/fresh subpolar and warm/saline subtropical waters. It is this interaction between these two water masses that results in the formation of these rotating features or eddies. Over time, the North Atlantic Current changes its pathway and alters the amount of subtropical versus subpolar water masses reaching the Iceland Basin. This difference in the water masses changes the dynamics at this front, such that when more subtropical waters reach the basin, the instabilities are more pronounced, resulting in an increased number of anticyclonic eddies, and vice versa.

1. Introduction

Mesoscale oceanic eddies play an important role in climate variability as they transport mass, heat, salt, and carbon around the world ocean and our knowledge about these features has grown tremendously since the advent of satellite altimetry. The Iceland Basin (IB) in the eastern Subpolar North Atlantic (SPNA) is an eddy-rich region with the most intense mesoscale eddy activity. The coupled interaction between North Atlantic Current (NAC) passing through IB and the mesoscale eddies along the subpolar front in the IB have recently been estimated to explain 50% of the variability in meridional heat transport (Zhao, Bower, Yang, Lin, & Penny Holliday, 2018). Mesoscale eddies in the IB thus play a critical role in the Atlantic Meridional Overturning Circulation (AMOC). However, how the eddy field in the IB, especially that of coherent eddies, has varied over the altimetry era and how it is linked to the pronounced decadal-scale climate variability of the SPNA (Chafik et al., 2016, 2019) remains poorly understood.

Previous studies on coherent eddies in the IB have mainly focused on the characteristics and generating mechanisms of individual eddies. For example, the PRIME eddy (Martin et al., 1998) observed in 1996 in the IB at 59.1°N, 20°W was an Anticyclonic Eddy (AE) with a diameter of 120 km. This was a near-stationary eddy for a period of 8 months and had a strong barotropic component in the velocity profiles. By combining hydrographic measurements and vessel-mounted current estimates, Read and Pollard (2001) identified a quasi-stationary AE in the interior of the IB in 1988. This eddy was in the vicinity of the PRIME eddy observed by (Martin et al., 1998). A study on discrete eddies using looping RAFOS floats in North Atlantic by Shoosmith et al. (2005) observed a quasi-stationary AE that was trapped in the central part of IB around 56°N for a period of 14 months. Chafik et al. (2014) showed the deep-reaching influence of eddies present at this region from a ship-mounted Acoustic Doppler Current Profiler (ADCP) along a transect near 59.5°N. The data from the Nuka Arctica ship along this
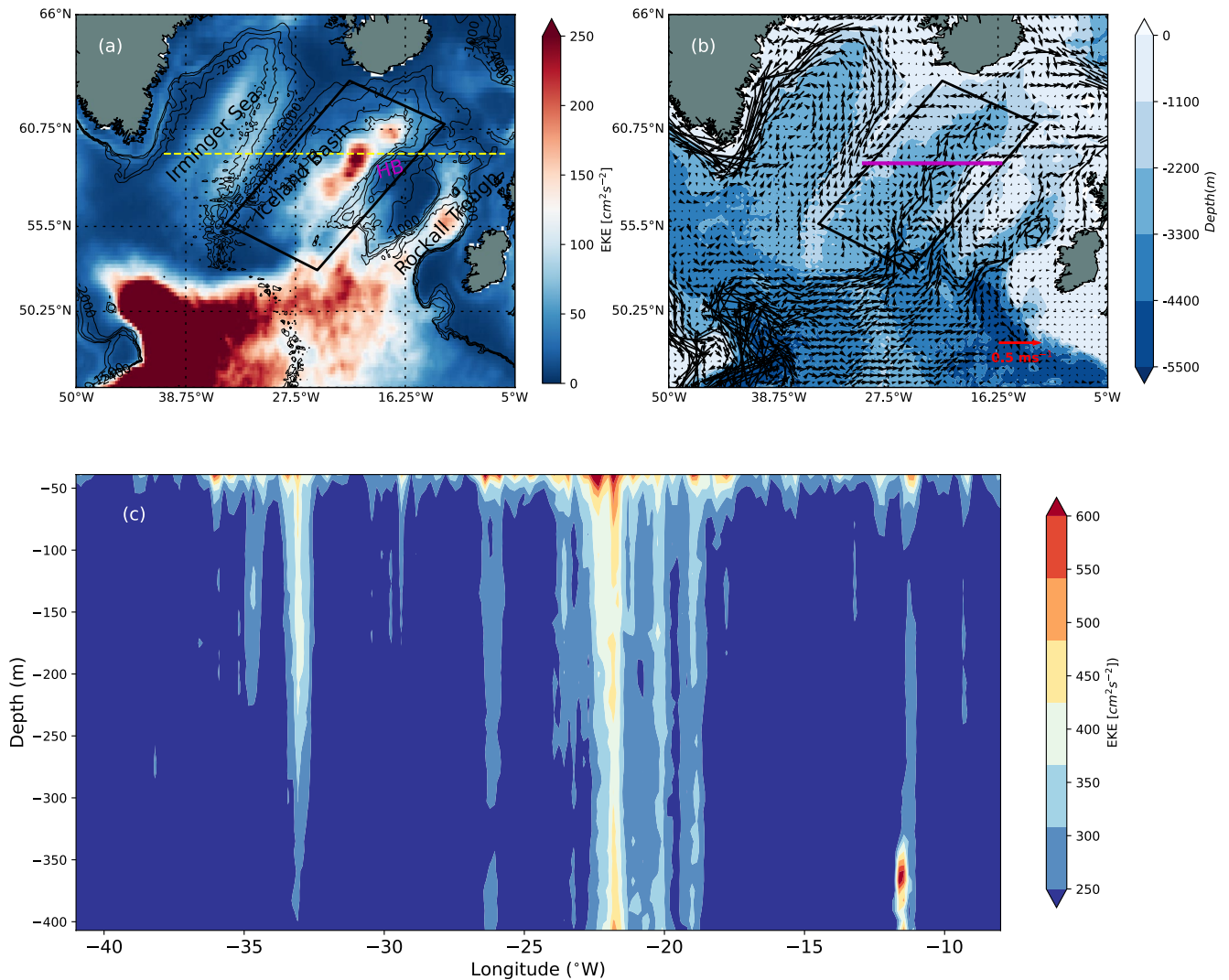
Figure 1. Map showing the 1993–2019 time-mean (a) EKE (cm² s⁻²) and (b) Geostrophic velocity vectors (m s⁻¹) in the subpolar North Atlantic overlaid with bathymetry data. HB stands for Hatton Bank in (a). The black box inside the map depicts the Iceland Basin (IB) and the black contours in (a) represents bathymetry. The magenta line in (b) is the transect passing through IB in Figures 5 and 6. (c) The mean eddy kinetic energy (cm² s⁻²) distribution as deduced from the Nuka Arctica ship transects during 1999–2002 along 59.5°N between 41 and 8°W as shown in the yellow dotted line in (a).

transect is reproduced in Figure 1c. Recently, Zhao, Bower, Yang, Lin, and Zhou (2018) documented the structure of an AE in the IB using high-resolution hydrographic and velocity observations, properties of which are consistent with previous studies in the region (Chafik et al., 2014; Martin et al., 1998; Read & Pollard, 2001; Shoosmith et al., 2005).

All these studies (Chafik et al., 2014; Martin et al., 1998; Read & Pollard, 2001; Zhao, Bower, Yang, Lin, & Penny Holliday, 2018) thus show the presence of a strong quasi-stationary eddy field in the IB near 58−60°N, 20−21°W, and different mechanisms for the eddy formation have been suggested. Martin et al. (1998) proposed the interaction between topography and the NAC as a mechanism for eddy generation. Read and Pollard (2001) attributed the existence and longevity of eddies in the IB to the variability of the subpolar gyre size, in turn, related to the NAC pathway. Shoosmith et al. (2005) hypothesized that westward meandering of the NAC generated eddies but did not explain their stationary nature. From hydrographic observations, Volkov (2005) suggested that hydrodynamical instability at the subpolar front is the primary source of mesoscale eddy field in the IB. High-resolution model simulations by Zhao, Bower, Yang, Lin, and Penny Holliday (2018) show that fluctuations in the zonal and vertical potential vorticity gradient near the seasonal and permanent pycnoclines create

the necessary conditions for barotropic and baroclinic instabilities for the formation of eddies in the IB. Using satellite maps Zhao, Bower, Yang, Lin, and Penny Holliday (2018) suggest that the eddy first appears near the slope region and later on moves westward to the central IB where it is trapped. These eddies, according to (Zhao, Bower, Yang, Lin, & Penny Holliday, 2018), are fed by the mean potential energy of the isopycnal slope at the subpolar front and by the mean kinetic energy of the NAC. It is worth mentioning that the common understanding is that AEs form and have the tendency to populate basins with topographic depressions such as the Lofoten Basin in the Nordic Seas, as recently demonstrated in numerical experiments by Solodoch et al. (2021). However, none of these studies discussed the long-term variability of formation and characteristics of coherent eddies. Our study focuses on reducing this knowledge gap.

An important element of the basin-scale circulation in the SPNA is the NAC, which splits east of the Mid-Atlantic Ridge and heads northeastward through the IB, Rockall Plateau, and Rockall Trough (Houpert et al., 2018). The mean geostrophic velocity field for the 1993–2019 period (Figure 1b) shows that the NAC through the IB has two parallel pathways toward the north-east: the main and hence the stronger NAC branch passes through the central basin while the other branch passes through the western edge of the Rockall Plateau. These northward flowing branches of the NAC bring subtropical waters to the basin and separate the cold subpolar waters from the warm waters in the eastern SPNA. The presence of high EKE regions in IB are confined to this oceanic front (Figure 1a).

The developments in satellite mapping over the last three decades have improved our understanding of the dynamical characteristics, spatial and temporal distribution of mesoscale eddies, and their pathways (Morrow et al., 2004). Automatic eddy detection algorithms are employed to detect and track eddies on a global scale in the ocean. The detection algorithms use either physical (Okubo, 1970; Weiss, 1991) or geometrical properties (Chelton et al., 2011; Faghmous et al., 2015; Nencioli et al., 2010; Schlax & Chelton, 2016) or the combination of the two (Chaigneau et al., 2008) to detect eddies in the ocean. Our study thus uses satellite-derived Sea Level Anomaly (SLA) data to quantify the spatio-temporal variability and associated statistics of coherent AEs generated in IB using two automatic eddy detection schemes. One is based on (Faghmous et al., 2015) and the other is the eddy trajectory atlas product distributed by AVISO based on Chelton et al. (2011); Schlax and Chelton (2016).

We analyze the low-frequency variability in the formation of coherent AEs in the IB over the altimetry era (1993–2019) and examine underlying physical processes and how they link to the decadal climate variability in the North Atlantic. The relative contribution of various large scale oceanic and atmospheric processes are examined by applying composite and multi-regression analysis. Finally, a Lagrangian approach is adapted to back-trace particles from the IB to examine the importance of different water masses in the formation of coherent AEs in the IB.

2. Data and Methods

2.1. Satellite Altimeter Data and Automatic Eddy Detection

Altimetry data for the Sea level anomalies (SLA), geostrophic velocity anomalies (both referenced to the 1993–2012 period), and absolute geostrophic velocity fields were obtained from the Copernicus Marine and Environment Monitoring Service (CMEMS; http://marine.copernicus.eu). SLA is the sea surface height above mean sea level. This data has a spatial resolution of $\frac{1}{4}°$ at daily intervals from 1993 through 2019. The Eddy Kinetic Energy (EKE) is calculated using, $EKE = \frac{u_g'^2 + v_g'^2}{2}$, where u_g' and v_g' are zonal and meridional components of the geostrophic velocity anomalies.

For the eddy detection and tracking, two products are employed for robustness. First is the altimetric Mesoscale Eddy Trajectories Atlas (META2.0) produced by SSALTO/DUACS and distributed by AVISO+ (https://aviso.altimetry.fr) with support from CNES, in collaboration with Oregon State University with support from NASA, hereafter AVISO. Spatially high-pass filtered "two-sat-merged" SLA maps were used for identifying eddies in this product. This algorithm identifies anticyclonic eddies by locating the pixel at a local maximum of SLA and successively finding all neighboring pixels with SLA values decreasing following the "growing method" of (Schlax & Chelton, 2016). AEs with amplitude less than 1 cm are not included in this product, the details of the algorithm can be found in (Chelton et al., 2011; Schlax & Chelton, 2016). The AVISO atlas provides the type

(cyclonic/anticyclonic), speed, radius, and associated metadata for the eddy. The second product is based on an automatic eddy detection algorithm by Faghmous et al. (2015), applied on the SLA data, hereafter FA15. This scheme look for an extremum defined as a grid cell whose SLA is greater (maximum) than its neighboring grids for an AE. The selection of the number of grids for the neighborhood depends on the requirements, here we chose a 3×3 neighborhood to account for the smaller eddies at higher latitudes. FA15 is a parameter free method since it does not impose any restriction on the minimum amplitude (difference in SLA between eddy center and the boundary) of the eddy to be detected. The eddy tracking procedure is applied for each eddy feature identified at time t, and look for the closest features at time $t + 1$ within a predefined search space based on the phase speed of long non-dispersive baroclinic Rossby waves, more details can be found in Faghmous et al. (2015).

2.2. Additional Data Sets

ARMOR3D data: This is a multivariate ocean state data downloaded from CMEMS; https://doi.org/10.48670/moi-00052. This data includes 3D Temperature, Salinity, Geostrophic Currents, available on a $\frac{1}{4}°$ regular grid and on 50 depth levels from the surface down to the bottom on a monthly scale. ARMOR3D combines satellite (SLA and sea surface temperature; SST) with in situ vertical profiles of temperature and salinity to build a global 3D dataset using statistical methods (Guinehut et al., 2012; Mulet et al., 2012). The monthly mean dataset used here covers 1993 through 2019. We used Gibbs-Sea Water (GSW) Oceanographic Toolbox (McDougall & Barker, 2011) to compute conservative temperature (Θ), absolute salinity (S_A), and potential density (σ_θ), from the ARMOR3D temperature and practical salinity. A subsurface metric used to calculate the position of Subpolar Front (SPF) uses salinity data obtained from monthly mean objectively analyzed hydrographic data set from the UK Met Office, EN4 (Good et al., 2013).

The Ocean Heat Content Anomaly (OHCA) fields (Levitus et al., 2012) for depths 0–700 m are downloaded from NOAA (https://www.ncei.noaa.gov/access/global-ocean-heat-content/heat_global.html). Monthly zonal and meridional wind stress used for calculating Wind Stress Curl (WSC) is downloaded from NCEP/NCAR Reanalysis (Kalnay et al., 1996; https://psl.noaa.gov/data/gridded/data.ncep.reanalysis.html). The spatial resolution of OHCA and WSC are $1 \times 1°$ and $1.875 \times 1.875°$, respectively. The data are then averaged into yearly means for the period 1993–2019 to perform the correlation analysis.

The North Atlantic Oscillation (NAO) index, the first leading mode of atmospheric variability in the SPNA, was provided by "The Climate Data Guide: Hurrell North Atlantic Oscillation (NAO) Index (PC-based)". Retrieved from https://climatedataguide.ucar.edu/climate-data/hurrell-north-atlantic-oscillation-nao-index-pc-based. The East Atlantic (EA) pattern index, the second leading mode of atmospheric variability, is downloaded from https://www.cpc.ncep.noaa.gov/data/teledoc/ea.shtml. Yearly means of NAO and EA index are used in this study. Finally, the mean EKE (1999–2002) data along Nuka Arctica ship transect between −41 and −8° W at 59.5°N latitude is obtained from (Chafik et al., 2014).

2.3. TRACMASS

We employ a mass conserving Lagrangian trajectory code TRACMASS to track the changes in the pathways of water in the North Atlantic using surface geostrophic velocity fields. Details of the new version of the TRACMASS model can be found in (Aldama-Campino et al., 2020) and is downloaded from https://www.tracmass.org/.

3. Results and Discussion

3.1. Characteristics and Distribution of Coherent AEs in the IB

Here, we discuss the characteristics, pathways, and spatiotemporal variabilities of the AEs in the IB from both AVISO and FA15 outputs. We have only considered AEs generated and stayed in the IB (black box in Figure 1a,b) for at least 7 days with a minimum lifespan of 28 days. A total of 1,242/1,021 AEs were detected by FA15/AVISO products between 1993 and 2019. The mean characteristics of the AEs are shown and compared in Table 1. FA15 recorded on an average 46 AEs per year which is 10 more than AVISO. The minimum (0.9/1.4 cm), maximum (14/17 cm), and the mean amplitude (4.6/5.2 cm) of AEs detected by FA15/AVISO indicate that the AVISO

Table 1
Characteristics of the Anticyclonic Eddies (AEs) From the Two Eddy Tracking Products Between 1993 and 2019

Parameters		FA15	AVISO
Number of AEs	Total	1242	1021
	per year	46 ± 6	36 ± 8
Amplitude (cm)	min	0.95	1.44
	avg	4.6 ± 2.3	5.2 ± 2.8
	max	14.0	17.0
Radius (km)	min	37	31
	avg	53 ± 8	51 ± 8
	max	96	91
Eddy life (days)	avg	51 ± 29	52 ± 29
	max	289	299
Direction of movement in%	North-West	36	30
	South-West	35	35
	North-East	21	22
	South-East	8	13
Distance between start and end point (km)	avg	68 ± 46	96 ± 67
	max	366	537

Note. ± represents the standard deviation.

method captures eddies with larger amplitudes. The AVISO method has a higher threshold step (1 cm) when looking for closed a contour of SLA lower than the AE center (highest local maximum of SLA). Therefore AVISO detects only AE that have at least 1 cm of amplitude at the eddy center. But for FA15 the threshold step is 0.05 cm, this results in more accurate eddy sizes and amplitudes. This difference can be observed in the eddy sizes, the minimum and maximum radius measured by FA15/AVISO are 37/31 km and 96/91 km, respectively. This difference between the two products is less obvious for the average eddy radius, that is, 53 and 51 km FA15 and AVISO, respectively. Since we have considered only eddies above 4 weeks of lifespan, the average lifespan of AEs detected are 51/52 days, and the longest AE detected has a lifespan of 289/299 days in FA15/AVISO. The average distance between the start and endpoint of the AEs were higher in eddies detected by the AVISO method, and nearly 71%/65% of the AEs moved westward in FA15/AVISO (see Table 1).

We conclude that the differences in the count and characteristics of the AEs obtained from FA15 and AVISO is most likely due to the dissimilarities in the eddy detection algorithms mentioned above and also the input satellite-derived SLA data used; while AVISO uses SLA derived from two satellites to be consistent throughout the detection, FA15 uses the multi-satellite product as this improves the detection. Despite these differences, the average amplitude (±1.1 cm), radius (±2.3 km), and life span (±2 days) of AEs were more or less similar in both products.

3.2. Spatial Variability of Coherent AEs in the IB

In this section, we focus on the spatial distribution of AEs in the SPNA. Figure 2a/b shows the AE density distribution represented by the number of coherent AEs passing through a grid per year for AVISO/FA15 respectively. A general feature from the two products is that the eddy density is concentrated along the NAC pathways through the basin (Figure 1b) and bears a strong similarity to the time-mean EKE field (Figure 1a). However, AVISO failed to capture the time-mean EKE pattern in IB.

To learn more about the formation and decay of coherent AEs in IB, we used start and endpoints of 1021/1242 eddies detected by AVISO/FA15. The frequency distribution of initial positions of AEs in the IB (Figure 2c,d) shows that AEs are generated in almost every region inside the basin with a higher frequency of occurrence in
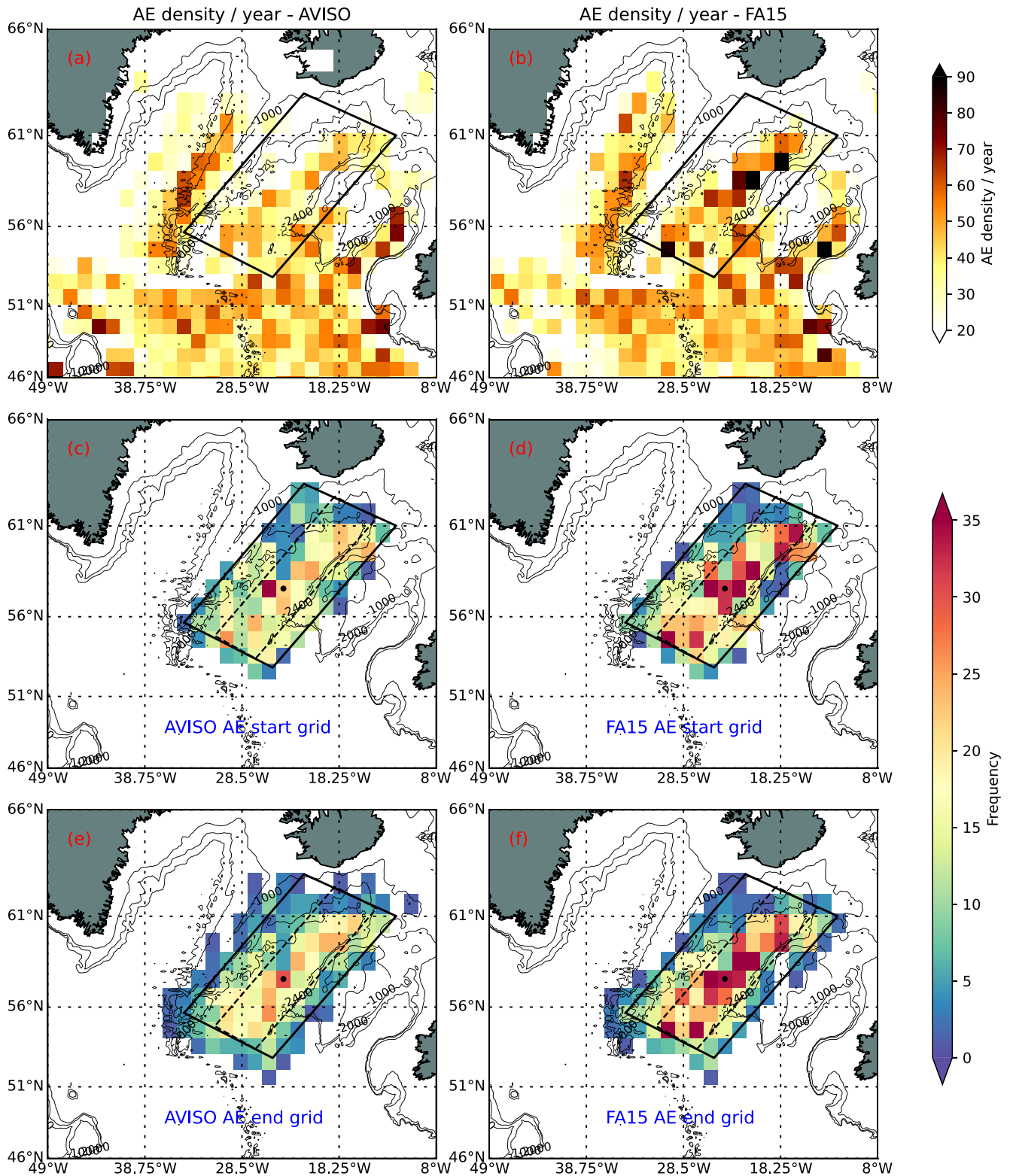
Figure 2. (a/b) Spatial distribution of eddy density per year in the SPNA based on FA15/AVISO (1 × 1.5° grid). Frequency distribution of (c/d) initial positions and (e/f) final positions of AEs from FA15/AVISO. The 1993–2019 period is used for all panels. The black box represent the Iceland Basin (IB), the black dotted box inside this covers the parts of the basin which are deeper than 2,400 m in panels (c–f). The black dots depict the center of mass of the frequency distribution in panels (c–f). Gray contours in the background in all the panels represent isobaths.

the deep basin, within the black dotted box (deeper than 2,400 m). The number of AEs formed in the black dotted box accounts for nearly 52%/60% of the total AEs detected by AVISO/FA15.

A closer look at these frequency distributions (Figure 2 c,d) shows that there are three hotspots: along the NAC pathway into the IB entry, the center of the IB, and near the IB exit. The central IB, that is, between 57 and 59°N, 21–26°W, is the region with the highest eddy generation. The center of mass of the frequency distribution (black dot in Figure 2c) coincides at the same point (24.125°W, 57.625°N) for both products. This further agrees with previous work highlighting the vigorous eddy activity in the central IB (Chafik et al., 2014; Martin et al., 1998; Read & Pollard, 2001; Zhao, Bower, Yang, Lin, & Zhou, 2018). Using hydrography and high-resolution numerical simulations Zhao, Bower, Yang, Lin, and Zhou (2018) proposed that topographic steering of the NAC along the western slopes of the Hatton bank is a viable cause for the eddy generation in this region. The AEs formed in the southeast corner of the IB accounts for nearly 9%/8% of the total eddy counts in AVISO/FA15 products. This could be attributed to the instabilities arising from the retroflection of the NAC before entering the IB (Hansen & Østerhus, 2000; Otto & Van Aken, 1996).

The frequency distribution of the final positions of AEs (Figure 2e, f) roughly matches the distribution of start points, with a slight westward shift: Nearly 71%/65% of the AEs detected by FA15/AVISO moved westward; see Table 1. The westward drift of the majority of the identified eddies is qualitatively consistent with the prevailing westward propagation of ocean eddies at speeds near that of long baroclinic Rossby waves reported by Chelton et al. (2007). However, the center of mass of the frequency distribution of both initial (Figure 2c, d) and final (Figure 2e, f) positions remained unchanged. This could be due to the entrapment of the westward moving AEs in the central basin, which are generated in the slopes of Hatton bank and the southeast corner of IB. Moreover, the central basin registered a 1.2/1% increase in frequency distribution for FA15/AVISO, respectively. The spatial distribution of initial and final positions of AEs does not, however, provide any information on the eddy pathways. The details of the eddy tracks are provided in the supplementary material (Figure S2 in Supporting Information S1).

The first baroclinic Rossby radius of deformation in the Iceland Basin (IB) ranges between 10 and 20 km. Since we are using a dataset with a resolution of $\frac{1}{4}°$ mesoscale flow features are not fully resolved in this product. The average radius of AEs in the IB reported in previous studies ranged between 40 and 60 km (Martin et al., 1998; Read & Pollard, 2001; Shoosmith et al., 2005; Zhao, Bower, Yang, Lin, & Zhou, 2018). The average radius (50–55 km) of the AEs detected in our analysis (Table 1) falls within this range. According to Zhao, Bower, Yang, Lin, and Zhou (2018), the average radius of the AEs observed in the IB are significantly larger than in any other basin in the SPNA. They suggested that barotropic instability of the NAC could be a possible reason for the large eddy sizes in the IB. Although our satellite-altimetry analyses miss some of the smaller eddies, they should still capture the essence of the long-term variability of eddy formation.

3.3. Temporal Variability of Coherent AEs in the IB

We have found a general geographical pattern of the time-averaged spatial distribution of AEs, and we now go on to examine how their occurrence vary from seasonal to decadal timescales. Since our interest is the low-frequency variability, we computed the yearly number of AEs generated in the IB. For eddies that span over 2 years, we sorted them into the year they existed for the highest number of days. The interannual variation of the count of the eddies between 1993 and 2019 based on FA15 and AVISO are displayed in Figure 3. All the correlations and trends calculated here are significant at the 95% confidence level ($p < 0.05$). During the 1994–2005 period, the number of AEs showed an upward trend (nearly 1 eddy per year both) reaching a maximum of 57/55 in 2005, thereafter the count of AEs decreased (nearly 1.4 eddies per year for both) to 31/27 in 2016 for FA15/AVISO. The correlation between the FA15 and AVISO time series on interannual scales is 0.42, while on decadal scales (using a 3-year running mean) it is 0.72.

Figure 3 further shows that the increasing and decreasing trends were not monotonous but rather intercepted by strong interannual variations in the count of AEs. Note also that the linear trends in the first (1993–2005) and second (2005–2016) decade were different: during the first period, the linear trend was 1.1/1 eddies per year, while for the second period it was −1.5/−1.4 for FA15/AVISO, significant at $p < 0.05$. Using mooring and glider observations between 2002 and 2009 Fan et al. (2013) found that the number of AEs increased almost threefold in

Figure 3. Yearly count of AEs in the IB during the 1993-2019 period from FA15 (Blue) and AVISO (Orange) product. Dashed thick lines represent the 3-year running mean in order to highlight the decadal-scale variability. The shaded region shows the standard error of the time series. The correlation coefficient between these two decadal time series based on these two different eddy tracking algorithms is 0.72, significant at $p < 0.05$.

occurrences between 2003 and 2005 followed by a period of the lower count. This could be a basin wide phenomenon, suggesting that the decadal ocean heat content in the SPNA are likely to play a role for the number of AEs. The high/low number of AEs coincide with the warming period (1993–2004)/cooling period (2005–2016) in the SPNA (Chafik et al., 2019). In fact, after 2016, the number of AEs started increasing again (Figure 3), a change that could be explained by the new warming phase in the SPNA, as recently reported by Desbruyères et al. (2021). It is interesting to note that the yearly number of Cyclonic Eddies (CEs) in the IB did not show this low-frequency variability (cf. Figure S3 in Supporting Information S1).

The amplitude and radius of the AE from the FA15 product showed a similar low-frequency variability as the number of AEs, increase during the first half reaching a maximum in the mid-2000s followed by a decrease in trend. However, this was absent in AVISO. Moreover, eddy's life did not show any such patterns in both products (cf. Figure S4 in Supporting Information S1). This may be because we have set a hard line on the minimum life to be 28 days. The number of AEs and eddy radius showed significant correlation in FA15 but, none of the parameters had any significant correlation with AVISO time series (cf. Figure S5 in Supporting Information S1).

The following section provides a detailed discussion of the large-scale patterns linked to the number of coherent AEs in the IB from FA15 as this eddy tracking algorithm is found to be more effective and realistic than that of AVISO. The selection of FA15 is based on the fact that it has the facility to adjust the threshold step (Section 3.1) whereas, in AVISO it is fixed. This results in wrong eddy size measurement and missing of weaker eddies in the later. While AVISO uses SLA derived from two satellites, FA15 uses the multi-satellite product as this improves the detection. Moreover, a seasonal pattern of eddy generation that is consistent with seasonal EKE is observed in FA15 which is absent in AVISO (cf. Figure S1 in Supporting Information S1). The process of selecting the FA15 in our analysis is further explained in the Supporting Information S1.

3.4. Linking Large-Scale Patterns to Coherent AEs

The large-scale oceanic and atmospheric conditions elsewhere can influence the regional circulation in the SPNA (Chafik et al., 2016). Here, we examine how the dynamics of AEs in the IB are linked to basin-scale oceanic and atmospheric patterns of variability to put our results in a larger-scale perspective.

A spatial correlation study has been carried out between the yearly number of AEs in the IB with yearly means of sea level (SLA), ocean heat content (OHC), and wind stress curl (WSC) anomalies at every grid point within the limit of 30–70°N and 70–0°W (Figure 4). We note that variations of SLA, OHC, and WSC are expected to be partly correlated via steric-height effects. SLA and OHC tend to be positively correlated and WSC tend to be negatively correlated via Ekman pumping. Figure 4 a, shows that sea level changes in SPNA/Subtropic North Atlantic (STNA) vary positively/negatively with the number of AEs. The correlation coefficient (r) ranged between −0.71 and 0.75, with the highest positive values in Irminger Sea and IB. The grid points where the r value is insignificant ($p > 0.05$) are marked with black dots in all panels of Figure 4. The OHC anomalies also behaved in the same manner as SLA with highest positive values of r (0.75–0.78) in the IB. However less regions in the STNA were negatively correlated with the number of AEs. Regarding the WSC, the number of AEs is negatively/positively correlated with WSC in SPNA/STNA respectively. The correlation values were lower (−0.5 to −0.61) compared to OHC and SLA.

Correlation does not guarantee causation, therefore we did a composite analysis to see how the parameters differ in periods of high and low number of AEs. Composites are calculated for years when the standard deviation (σ) of the number of AEs has exceeded a certain limit ($>0.75\sigma$). A composited difference is plotted in Figure 4 d,e,f to understand the structural characteristics of SLA, OHC, and WSC in high and low periods. A similar pattern is seen when using composite analysis. However, a more pronounced negative SLA is observed in the western subtropical North Atlantic, especially along the NAC path and in the Gulf Stream region (not shown) reflecting the dipole nature of SLA variability in North Atlantic Figure 4d. The variability of OHC in the SPNA covaries with Atlantic Multidecadal Variability, which in turn, is modulated by northward advection of subtropical waters, where wind stress changes are likely to play a role (Broomé et al., 2020; Chafik et al., 2016, 2019; Desbruyères et al., 2021; Häkkinen et al., 2013). When it comes to WSC, the composite difference shows a dipole structure similar to the negative phase of the North Atlantic Oscillation (the leading mode of atmospheric variability in the North Atlantic). The results from both correlation and composite analysis point out that the number of AEs in IB is higher when the SLA and OHC in the SPNA are higher, and there could be a positive feedback between these two. WSC behaves exactly opposite to this. We also note that during years of high AEs, the zero WSC (magenta contour in Figure 4f) shifts further north into the IB, allowing more subtropical waters to be advected into the basin. This leads to changes in the water-mass properties in the IB and will be discussed next.

3.5. Linking Water Mass Changes and Subpolar Front Shifts to Coherent AEs

We have considered a transect in the SPNA for the mean latitudinal band (58–60°N) to see how salinity and temperature change in the periods of high and low states of AEs ($>0.75\sigma$). Figure 5 shows the composite difference of absolute salinity (S_A) and conservative temperature (Θ), between high and low states from ARMOR3D data. The maximum composited difference of the salinity and temperature is 0.17 g/kg and 1.43°C, respectively, in the IB region of the transect. The composite differences in hydrography reflect a westward shift of the subpolar front in periods with an anomalously high number of AEs, which can be inferred from the individual high and low composites (not shown). In general, from the composite difference (Figure 5), we infer that years with a high number of AEs in the IB coincide with warmer and more saline conditions than during years with a low number of AEs. The lower number of eddies seen in our study have occurred between 2012 and 2016 (Figure 4), that is, during the recent rapid freshening of the eastern SPNA (Holliday et al., 2020). The freshening signal reached the IB in 2015 and intensified in the top 1,000 m depth in 2016 which were years with the least number of AEs observed. The subpolar front (SPF) in the IB is located where the main branch of NAC passes (Desbruyères et al., 2021). Therefore, we hypothesize that the relative position of the NAC in the IB controls the proportion of warmer and saline subtropical versus cooler and fresher subpolar waters play a role in the number of AEs in the IB.
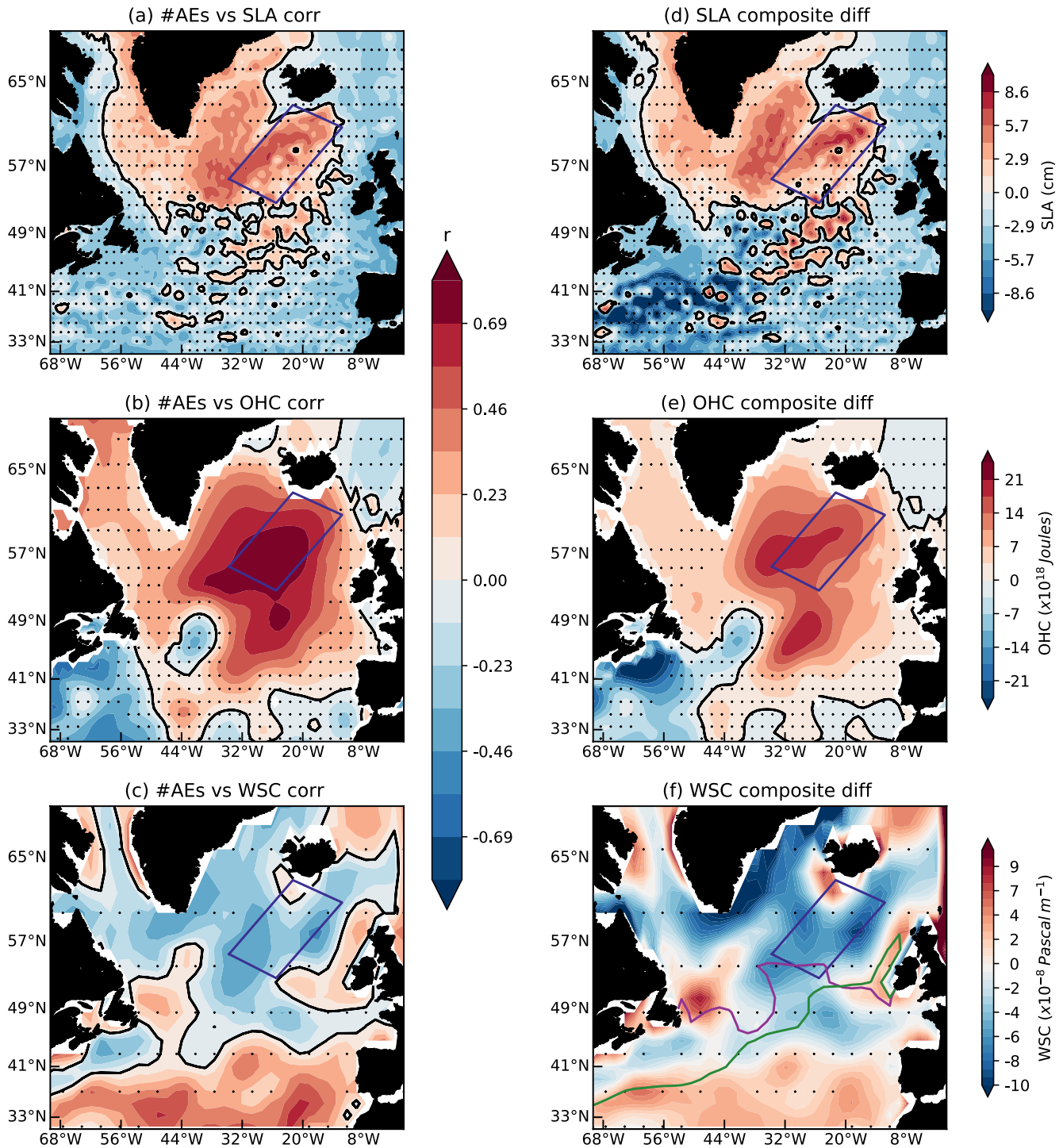
Figure 4. Spatial correlation maps of the yearly number of AEs against (a) Sea Level Anomaly (SLA), (b) Ocean Heat Content (OHC) (c) Wind Stress Curl (WSC). Composite difference of (d) SLA, (e) OHC, (f) WSC based on anomalously high minus anomalously low years of the number of AEs using 0.75 standard deviations as the threshold value. The stipplings indicate non-significant regions at the 95% confidence level. Significance of the difference for the composites is tested with a two-tailed t-distribution following (Häkkinen & Mo, 2002). The blue box inside each sub-figure denotes the IB. Zero contour line is represented by the black contours in (a,b,c,d,e). The magenta (green) contours in (f) depicts the zero WSC during high (low) periods.
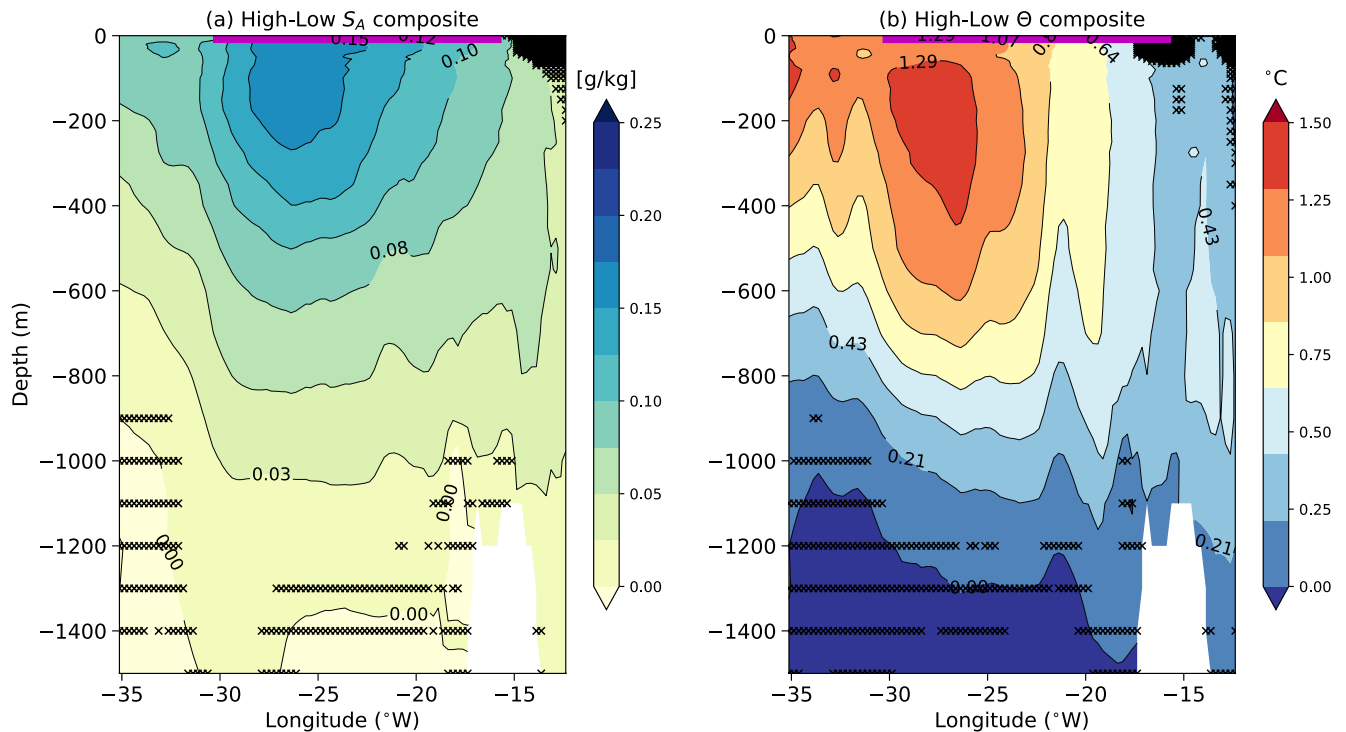
Figure 5. (a) Composite difference of absolute salinity at the mean latitudinal band between 58 and 60°N in the SPNA between −35 and −12°W based on periods of high minus low AEs. (b) Same as (a) but for conservative temperature. The thick magenta line on top of (a) and (b) represents the transect covering the Icelandic Basin as shown in Figure 1. The stipplings indicate the regions that are not significant at 95% confidence level.

The Hovmöller diagram in Figure 6a, represents the timeline of the magnitude of the surface geostrophic velocity in longitudinal transect of the NAC (in the mean latitudinal band 58–60°N). The velocity of the NAC was highest during the early 2000s and the mid-2000s with a marginal westward intensification in the 2004–2005 period. The strength of the main branch of NAC was weaker before and after the 2000s. Moreover, a noticeable eastward shift in the current was observed after 2010. When corroborating with the number of AE formations in the IB we see a similar pattern that is, the highest number of eddies were observed in the early 2000s and mid-2000s when the NAC was stronger and had a marginal westward shift. The number of eddies were lowest during 2015–2016 when there was an eastward shift in the current and a weaker NAC through the central basin.

The results presented in Figure 4 suggest that a link between the generation of anticyclonic eddies in the IB, and the flow field in the subpolar North Atlantic. To examine this, we employ a Lagrangian experiment to identify the time variations in the pathways that feed the the NAC in the eastern IB. For this purpose, particle tracking of surface trajectories has been done using the Lagrangian code TRACMASS (Aldama-Campino et al., 2020) from daily surface geostrophic velocities. The periods selected for this experiment are 2005–2004 and 2016–2015, that is, the periods when the number of anticyclonic eddies are highest and lowest, respectively. The experiment is based on the release of around 500 particles per day in a region between 25 and 12°W for the first 31 days along a transect at 60°N (Figure 7). In total, we have back-traced 16,740 particles for both periods and calculated the percentage of trajectories passing through two sections in the western SPNA and the subtropics (Figure 7). During periods of lower number of AEs, 30/9% of the particles came from subpolar/subtropical section, however in periods of the higher number of AEs the count changed to 12/17%, respectively. This shows that during 2004–2005 (high number of AEs) nearly two times of particles reached IB from subtropics compared to the 2015–2016 (low number of AEs) period.

The results summarized in Figure 7 suggest that the variability in the generation of AEs may be caused by changes of the baroclinicity and strength of the NAC, which may vary with abundance of subtropical water. To investigate this, we have calculated the Eady growth rate (EGR), which is a measure of baroclinic instability. The EGR is defined as $\sigma_e^{\max} = 0.3 \frac{|\mathbf{U}_{tw}|}{L_d}$, where $\mathbf{U}_{tw}$ is the magnitude of the top-to-bottom thermal wind shear and L_d is

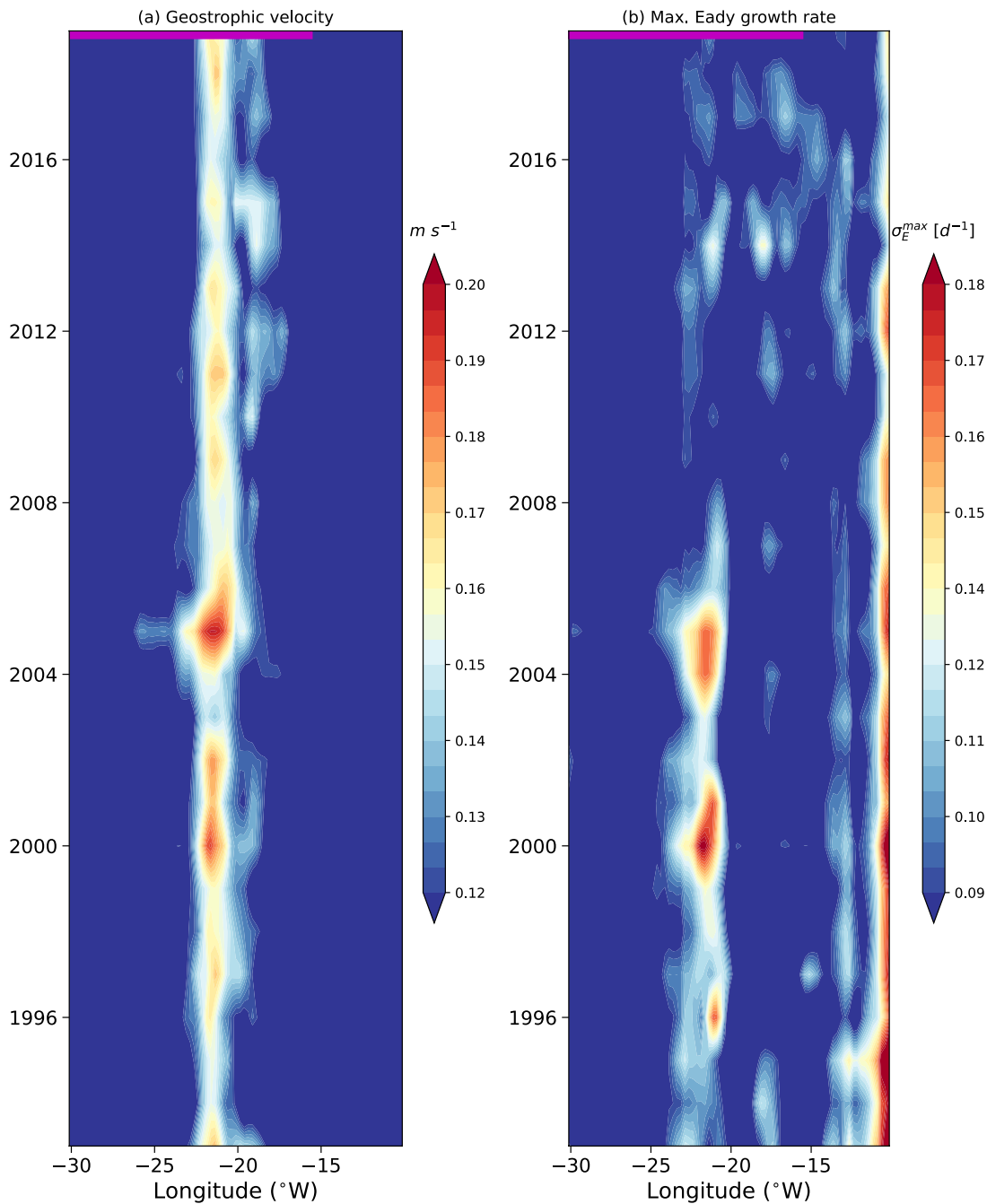**Figure 6.** (a) Hovmöller diagram of the magnitude of surface geostrophic velocity field along a transect between −30 and −10°W for a mean latitudinal band 58–60°N from the satellite altimetry. (b) Maximum Eady growth rates [day^{-1}] based on ARMOR3D data from CMEMS along the same transect from 1993 to 2019. The magenta line on top represents the section covering the Icelandic Basin as shown in Figure 1.

the first internal deformation radius (Isachsen, 2015). Figure 6b, shows the EGR calculated in the same transect as in Figure 6a from the ARMOR3D dataset from CMEMS. The EGR is a rough measure of how conducive the time-mean flow is to generate eddies growing via baroclinic instability. The east–west variation of the EGR delineates zones with strong baroclinicity, where eddies are likely to form. Generally, higher EGR values are encountered along the path of NAC and toward the western edge of the Rockall Plateau. Moreover, the highest values of the EGR occurred during 1999–2006, when the NAC was strong and confined to the center of the basin. When the NAC shifted eastward after 2010, the EGR values reduced along the main current pathway, and regions
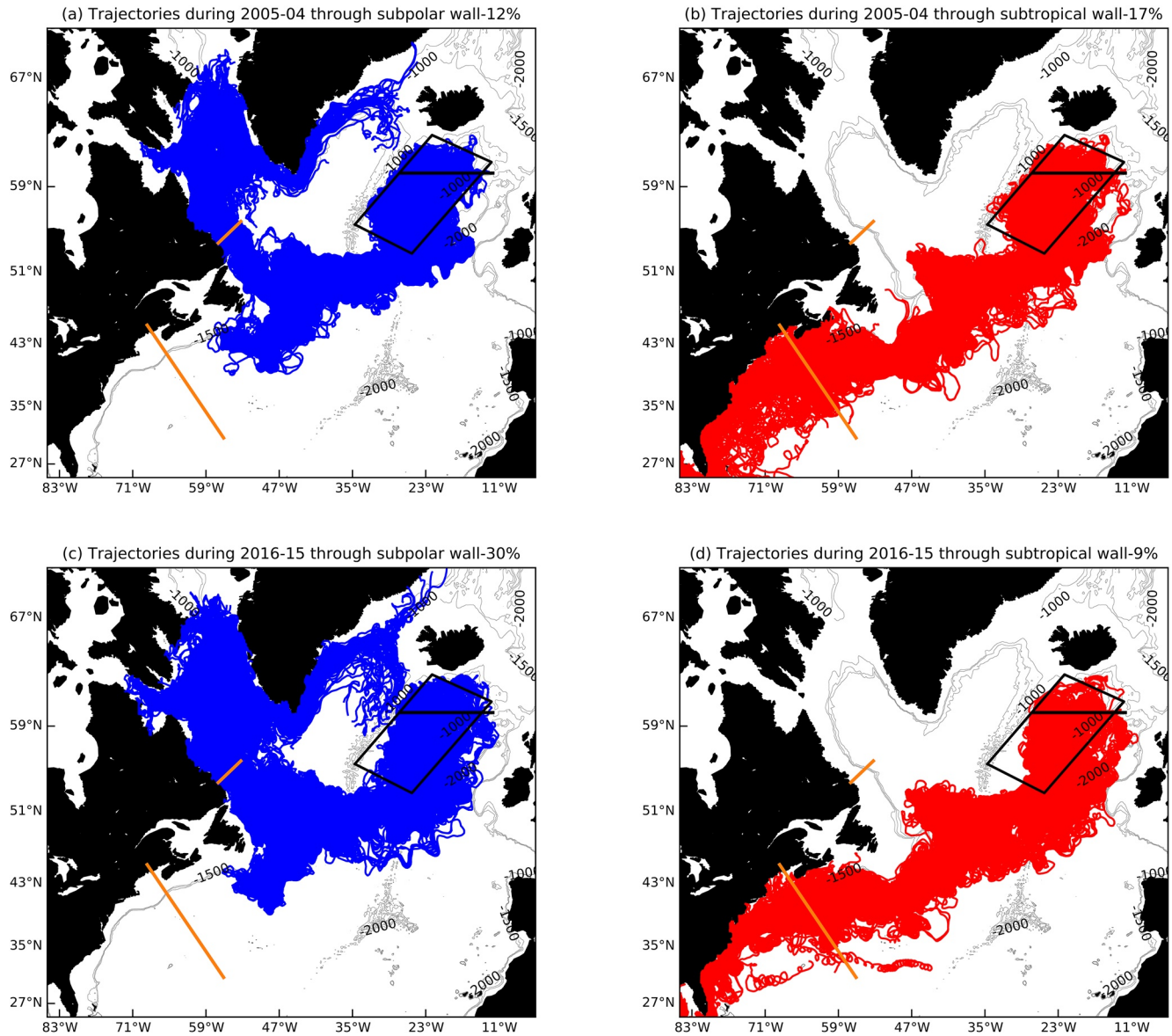
Figure 7. Trajectories back traced from a section between 27 and 12°W at 60°N in the IB (thick black line) for two years during two separate periods using geostrophic velocities. The number of trajectories heading to North-West (South-West) are counted across a section represented by orange lines. (a), (b) Trajectories passing through NW (SW) transect during 2005–04 period respectively. (c), (d) same as (a), (b) but for 2016–15 period. Gray contours in the background represent the bathymetry and the black box covers the IB. The percentage of particles that reached either the NW or SW transect from IB during this experiment is given in the title of each panel.

with weaker EGR values emerged to the east. These results support our hypothesis that the increased generation of AE in the IB from around 2000 to 2006 was linked to conditions of the NAC that were more conducive to the formation meso-scale eddies. Furthermore, this period coincided with the arrival of more subtropical waters, suggesting a link between the baroclinicity of the NAC in the IB and the abundance of subtropical waters.

To look further into this, we constructed a metric of the SPF based on the zonal position of isohaline at 250 dbar following Sarafanov et al. (2008). However, since there is a lack of coherent frontal shifts in the eastern SPNA (Foukal & Lozier, 2017), the location of SPF varies with the latitude of our choice. As a result, we have calculated the SPF based on the 35.3 isohaline at 250 dbar from mean salinity data from EN4 dataset between 53 and 62°N latitudinal band (note that this SPF metric covaries with that based on the 35.0 isohaline used in Sarafanov et al. (2008) and Foukal and Lozier (2017)). The interannual/decadal westward shifts of the SPF is found to covary strongly with the number of AEs ($r = -0.73/-0.88$, $p < 0.05$), Figure 8. The number of AEs were highest
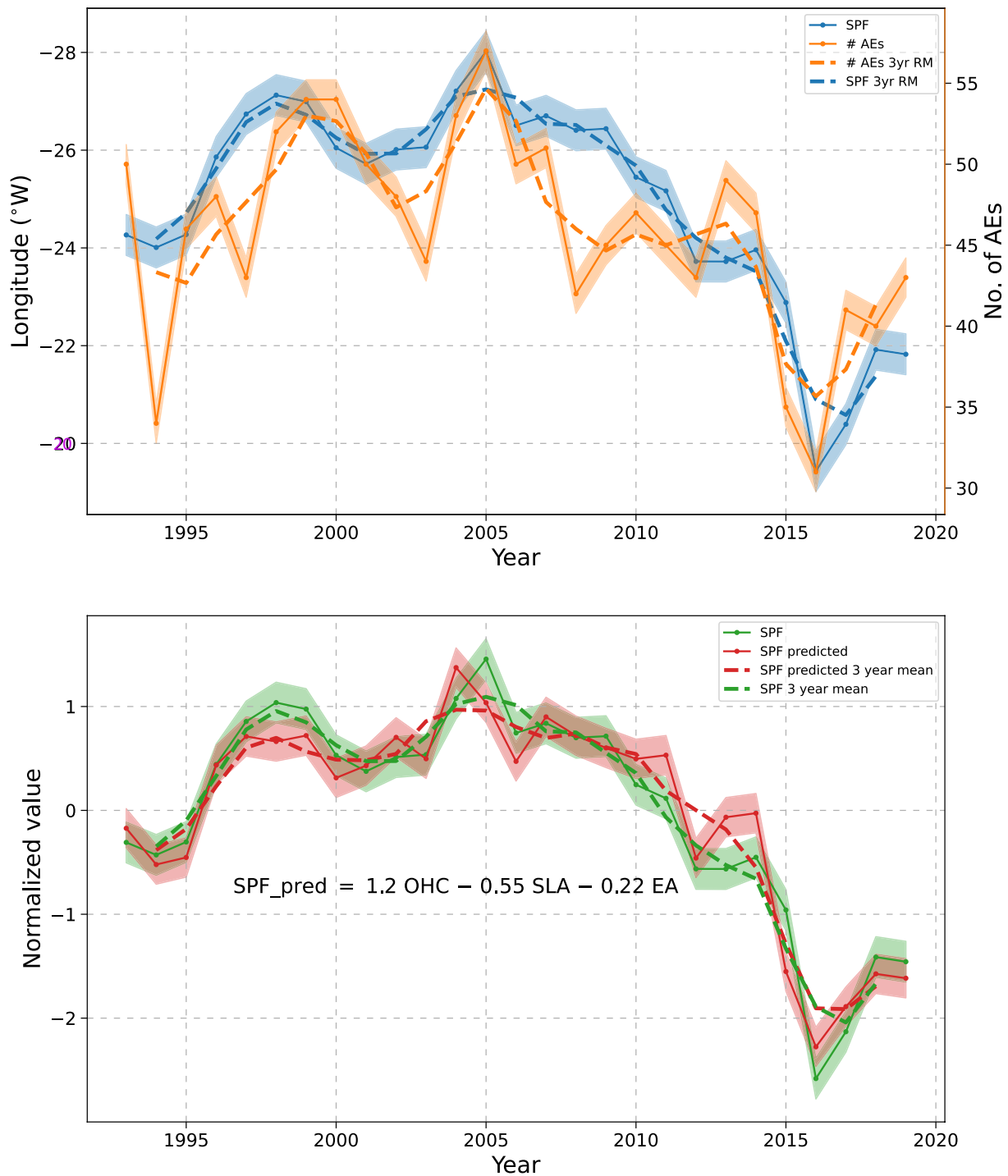
Figure 8. (a) Time series of no of AEs (Orange) versus the position of SPF (Blue) in the latitudinal band 53–62°N for the period between 1993 and 2019. The dotted lines represents the 3 years running means for the corresponding time series. The correlation coefficient (r) between yearly/3 years running mean time series of SPF and number of AEs is −0.73/−0.88 respectively. (b) Time series of SPF (Green) versus the predicted SPF (Red) from the multiple regression analysis for the period between 1993 and 2019. The dotted lines represents the 3 years running means for the corresponding time series. The coefficient of multiple determination (R^2) between 3 years running mean time series of SPF and predicted SPF is 0.96.

and lowest when the SPF was at its westernmost and easternmost position in 2005 and 2016, respectively. These 2 years are known for exceptionally warm (Häkkinen et al., 2011) and cold (Chafik et al., 2019) periods in the decadal variability of the SPNA.

3.6. A Multiple Regression Approach to Predict the Position of SPF in the IB

In Section 3.5, we found that SPF shifts can explain more than 53% and 77% of the variability in the AE formation in the IB on annual and decadal timescales, respectively. The SPF position in the IB is linked to the NAC paths, which, in turn, depend on multiple atmosphere-ocean processes. Thus, we perform a multiple regression analysis to quantify the relative skill of these factors in predicting the SPF position in the IB.

The variables considered here are OHC, SLA, North Atlantic Oscillation (NAO) index, and the East Atlantic (EA) pattern index. The selection of these variables is consistent with the analysis in Section 3.4. Note, however, that instead of the WSC we use the first two leading modes of atmospheric variability in the SPNA, namely the NAO and EA. OHC alone is found to be the main variable explaining most of the SPF variance ($R^2 = 0.70$), adding SLA to the first model improves the R^2 value to 0.89 (refer Table provided in the supplementary material). However, the addition of NAO did not improve the predictability of the SPF. Instead, if we select OHC, SLA, and EA as predictors in the regression model, we are able to predict 93% of the variability in the SPF, Figure 8b. EA and SLA are negatively correlated to the westward shift of the subpolar front position, whereas OHC is positively correlated.

It is interesting that the EA rather than the NAO, the leading mode of atmospheric variability, was found to significantly contribute to the multiple regression model and in predicting the SPF position. One possible reason is that the EA is a good indicator of the relative position of the WSC centers of action over the SPNA (e.g., Foukal and Lozier (2017)), which, in turn, via modulation of the WSC zero line (cf. Figure 5f) regulate the flow of subtropical waters into SPNA (Häkkinen et al., 2011). The contribution of the EA to the eddy count variability is exemplified in 2005 when the EA was strongly negative and the count of AEs were highest, although the NAO was positive.

4. Summary and Conclusion

Two automatic mesoscale eddy detection schemes (FA15 and AVISO) based on satellite altimetry were employed to study the characteristics, pathways, and spatiotemporal variability of the AEs in the IB between 1993 and 2019. FA15 method detected more than 200 AEs as compared to AVISO during this period. Moreover, the spatial density distribution of AEs in the FA15 matched the EKE pattern in the SPNA. The frequency distribution of formation and decay of coherent AEs in the IB from both methods shows that more than half of the total number of AEs are generated in the deep basin along the major NAC pathway, a view consistent with previous studies. Another major area of eddy generation is the southeast corner of the IB, which accounts for nearly 10% of the total eddy generation. Nearly 71/65% of the AEs detected by FA15/AVISO moved westward and the majority of the AEs generated in the eastern IB moved westward and ended up in the central basin. Our study thus documents, for the first time, the eddy statistics from two ocean eddy detection algorithms in the IB of the SPNA.

The interannual variation in the count of AEs based on these two ocean eddy detection schemes, FA15 and AVISO, between 1993 and 2019 showed a pronounced low-frequency variability matching the decadal trends previously observed in the SPNA. Although both methods captured a similar low-frequency variability, they failed to match on interannual time scales. The disparities in the count might have aroused from the differences in the algorithm and the type of SLA data (FA15 uses multi-satellite data while AVISO uses two satellite data) used for eddy detection. We have, therefore, relied mainly on FA15 when examining the observed linkages.

Linking the yearly count of AEs to the spatial patterns of key variables (SLA, OHC, and WSC) revealed that during periods of high and low number of eddies, the SLA/OHC was anomalously higher than during periods of low number of AEs. This difference was also evident in the subsurface salinity and temperature distributions, such that increased temperature and salinity coincide with a higher number of AEs. The relative position of the NAC in the IB, which modulates the position of subpolar front, was proposed as a factor that can explain these changes since it controls how much warm and saline subtropical versus cold and fresh subpolar waters reach the eastern SPNA. A Lagrangian approach was adopted to backward trace the origin of the particles from the IB which shows that during years of the high number of AEs, nearly twice the number of trajectories is found to reach the IB from the subtropics as compared to the years with the low number of AEs.

The EGR calculated along a transect in the IB shows, increased baroclinic instabilities in the frontal regions with the arrival of more subtropical waters in the early to mid-2000s. The interannual variation in the zonal position of the SPF based on the 35.3 isohaline is found to explain more than 53% of the variability in the number of AEs. On decadal timescales, it explains 77% of the variability. The number of eddies were highest when the SPF was at its westernmost position in 2005 and least in 2016 when the SPF was at its easternmost position in IB.

The present study shows, for the first time, that the formation of AEs in the IB is signified by low-frequency time scales. This variability depends largely on the relative position and strength of the NAC, and therefore also on the proportion of warm subtropical versus cold subpolar waters in the basin.

Conflict of Interest

The authors declare no conflicts of interest relevant to this study.

Data Availability Statement

The altimetry-derived eddy trajectories version 2.0 DT (AVISO) is downloaded from the value-added product section of AVISO /www.aviso.altimetry.fr. The FA15 eddy detection and tracking code is accessible from https://doi.org/10.5281/zenodo.13037. The Lagrangian code TRACMASS can be accessed from Zenodo, https://doi.org/10.5281/zenodo.4337926.

References

Aldama-Campino, A., Döös, K., Kjellsson, J., & Jönsson, B. (2020). Tracmass: Formal release of version 7.0 Version v7.0-beta. https://doi.org/10.5281/zenodo.4337926

Broomé, S., Chafik, L., & Nilsson, J. (2020). Mechanisms of decadal changes in sea surface height and heat content in the eastern nordic seas. *Ocean Science*, *16*(3), 715–728. https://doi.org/10.5194/os-16-715-2020

Chafik, L., Even, J., Nilsen, Ø., Dangendorf, S., Reverdin, G., & Frederikse, T. (2019). North Atlantic Ocean circulation and decadal sea level change during the altimetry era. *Scientific Reports*, *9*(1041). https://doi.org/10.1038/s41598-018-37603-6

Chafik, L., Häkkinen, S., England, M. H., Carton, J. A., Nigam, S., Ruiz-Barradas, A., et al. (2016). Global linkages originating from decadal oceanic variability in the subpolar North Atlantic. *Geophysical Research Letters*, *43*(2010), 10909–10919. https://doi.org/10.1002/2016GL071134

Chafik, L., Rossby, T., & Schrum, C. (2014). On the spatial structure and temporal variability of poleward transport between Scotland and Greenland. *Journal of Geophysical Research: Oceans*, *119*, 824–841. https://doi.org/10.1002/2013JC009287

Chaigneau, A., Gizolme, A., & Grados, C. (2008). Mesoscale eddies off Peru in altimeter records: Identification algorithms and eddy spatio-temporal patterns. *Progress in Oceanography*, *79*(2), 106–119. https://doi.org/10.1016/j.pocean.2008.10.013

Chelton, D. B., Schlax, M. G., & Samelson, R. M. (2011). Global observations of nonlinear mesoscale eddies. *Progress in Oceanography*, *91*(2), 167–216. https://doi.org/10.1016/j.pocean.2011.01.002

Chelton, D. B., Schlax, M. G., Samelson, R. M., & De Szoeke, R. A. (2007). Global observations of large oceanic eddies. *Geophysical Research Letters*, *34*(15). https://doi.org/10.1029/2007GL030812

Desbruyères, D., Chafik, L., & Maze, G. (2021). A shift in the ocean circulation has warmed the subpolar North Atlantic Ocean since 2016. *Communications Earth & Environment*, *2*(1), 48. https://doi.org/10.1038/s43247-021-00120-y

Faghmous, J. H., Frenger, I., Yao, Y., Warmka, R., Lindell, A., & Kumar, V. (2015). A daily global mesoscale ocean eddy dataset from satellite altimetry. *Scientific Data*, *2*(1), 150028. https://doi.org/10.1038/sdata.2015.28

Fan, X., Send, U., Testor, P., Karstensen, J., & Lherminier, P. (2013). Observations of irminger sea anticyclonic eddies. *Journal of Physical Oceanography*, *43*(4), 805–823. https://doi.org/10.1175/JPO-D-11-0155.1

Foukal, N. P., & Lozier, M. S. (2017). Assessing variability in the size and strength of the North Atlantic subpolar gyre. *Journal of Geophysical Research: Oceans*, *122*(8), 6295–6308. https://doi.org/10.1002/2017JC012798

Good, S. A., Martin, M. J., & Rayner, N. A. (2013). EN4: Quality controlled ocean temperature and salinity profiles and monthly objective analyses with uncertainty estimates. *Journal of Geophysical Research: Oceans*, *118*(12), 6704–6716. https://doi.org/10.1002/2013JC009067

Guinehut, S., Dhomps, A.-L., Larnicol, G., & Le Traon, P.-Y. (2012). High resolution 3-d temperature and salinity fields derived from in situ and satellite observations. *Ocean Science*, *8*(5), 845–857. https://doi.org/10.5194/os-8-845-2012

Häkkinen, S., & Mo, K. C. (2002). The low-frequency variability of the tropical Atlantic ocean. *Journal of Climate*, *15*(1), 237–250. https://doi.org/10.1175/1520-0442(2002)015<0237:tlfvot>2.0.co;2

Häkkinen, S., Rhines, P. B., & Worthen, D. L. (2011). Warm and saline events embedded in the meridional circulation of the northern North Atlantic. *Journal of Geophysical Research*, *116*(C3), C03006. https://doi.org/10.1029/2010JC006275

Häkkinen, S., Rhines, P. B., & Worthen, D. L. (2013). Northern North Atlantic sea surface height and ocean heat content variability. *Journal of Geophysical Research: Oceans*, *118*(7), 3670–3678. https://doi.org/10.1002/jgrc.20268

Hansen, B., & Østerhus, S. (2000). North Atlantic–Nordic seas exchanges. *Progress in Oceanography*, *45*(2), 109–208. https://doi.org/10.1016/S0079-6611(99)00052-X

Holliday, N. P., Bersch, M., Berx, B., Chafik, L., Cunningham, S., Florindo-López, C., et al. (2020). Ocean circulation causes the largest freshening event for 120 years in eastern subpolar North Atlantic. *Nature Communications*, *11*(1), 1–15. https://doi.org/10.1038/s41467-020-14474-y

Houpert, L., Inall, M. E., Dumont, E., Gary, S., Johnson, C., Porter, M., et al. (2018). Structure and transport of the north Atlantic current in the eastern subpolar Gyre from Sustained glider observations. *Journal of Geophysical Research: Oceans*, *123*(8), 6019–6038. https://doi.org/10.1029/2018JC014162

Isachsen, P. E. (2015). Baroclinic instability and the mesoscale eddy field around the Lofoten Basin. *Journal of Geophysical Research: Oceans*, *120*(4), 2884–2903. https://doi.org/10.1002/2014JC010448

Kalnay, E., Kanamitsu, M., Kistler, R., Collins, W., Deaven, D., Gandin, L., et al. (1996). The NCEP/NCAR 40-year reanalysis project. *Bulletin of the American Meteorological Society*, *77*, 4372–4471. https://doi.org/10.1175/1520-0477(1996)077<0437:tnyrp>2.0.co;2

Levitus, S., Antonov, J. I., Boyer, T. P., Baranova, O. K., Garcia, H. E., Locarnini, R. A., et al. (2012). World ocean heat content and thermosteric sea level change (0-2000 m), 1955-2010. *Geophysical Research Letters*, *39*(10), a–n. https://doi.org/10.1029/2012GL051106

Martin, A. P., Wade, I. P., Richards, K. J., & Heywood, K. J. (1998). The PRIME eddy. *Journal of Marine Research*, *56*(2), 439–462. https://doi.org/10.1357/002224098321822375

McDougall, T. J., & Barker, P. M. (2011). Getting started with TEOS-10 and the Gibbs Seawater (GSW) Oceanographic toolbox. *SCOR/IAPSO*, *WG127*, (p. 28).

Morrow, R., Birol, F., Griffin, D., & Sudre, J. (2004). Divergent pathways of cylonic and anti-cyclonic ocean eddies. *Geophysical Research Letters*, *31*(24), 1–5. https://doi.org/10.1029/2004GL020974

Mulet, S., Rio, M.-H., Mignot, A., Guinehut, S., & Morrow, R. (2012). A new estimate of the global 3d geostrophic ocean circulation based on satellite data and in-situ measurements. *Deep Sea Research Part II: Topical Studies in Oceanography*, *77–80*, 70–81. (Satellite Oceanography and Climate Change). https://doi.org/10.1016/j.dsr2.2012.04.012

Nencioli, F., Dong, C., Dickey, T., Washburn, L., & McWilliams, J. C. (2010). A vector geometry–based eddy detection algorithm and its Application to a high-resolution numerical model product and high-frequency radar surface velocities in the southern California Bight. *Journal of Atmospheric and Oceanic Technology*, *27*(3), 564–579. https://doi.org/10.1175/2009JTECHO725.1

Okubo, A. (1970). Horizontal dispersion of floatable particles in the vicinity of velocity singularities such as convergences. *Deep Sea Research and Oceanographic Abstracts*, *17*(3), 445–454. https://doi.org/10.1016/0011-7471(70)90059-8

Otto, L., & Van Aken, H. M. (1996). Surface circulation in the northeast Atlantic as observed with drifters. *Deep-Sea Research Part I Oceanographic Research Papers*, *43*(4), 467–499. https://doi.org/10.1016/0967-0637(96)00017-9

Read, J. F., & Pollard, R. T. (2001). A long-lived eddy in the Iceland Basin 1998. *Journal of Geophysical Research*, *106*(C6), 11411–11421. https://doi.org/10.1029/2000JC000492

Sarafanov, A., Falina, A., Sokov, A., & Demidov, A. (2008). Intense warming and salinification of intermediate waters of southern origin in the eastern subpolar North Atlantic in the 1990s to mid-2000s. *Journal of Geophysical Research*, *113*(12), 1–8. https://doi.org/10.1029/2008JC004975

Schlax, M. G., & Chelton, D. B. (2016). *The "growing method" of eddy identification and tracking in two and three dimensionscollege of earth*. ocean and atmospheric sciences, oregon state university

Shoosmith, D. R., Richardson, P. L., Bower, A. S., & Rossby, H. T. (2005). Discrete eddies in the northern North Atlantic as observed by looping RAFOS floats. *Deep-Sea Research Part II Topical Studies in Oceanography*, *52*(3–4), 627–650. https://doi.org/10.1016/j.dsr2.2004.12.011

Solodoch, A., Stewart, A. L., & McWilliams, J. C. (2021). Formation of anticyclones above topographic depressions. *Journal of Physical Oceanography*, *51*(1), 207–228. https://doi.org/10.1175/JPO-D-20-0150.1

Volkov, D. L. (2005). Interannual variability of the altimetry-derived eddy field and surface circulation in the extratropical North Atlantic Ocean in 1993-2001. *Journal of Physical Oceanography*, *35*(4), 405–426. https://doi.org/10.1175/JPO2683.1

Weiss, J. (1991).)The dynamics of enstrophy transfer in two-dimensional hydrodynamics. *Physica D: Nonlinear Phenomena*, *48*(2–3), 273–294. https://doi.org/10.1016/0167-2789(91)90088-Q

Zhao, J., Bower, A., Yang, J., Lin, X., & Penny Holliday, N. (2018). Meridional heat transport variability induced by mesoscale processes in the subpolar North Atlantic. *Nature Communications*, *9*(1), 1124. https://doi.org/10.1038/s41467-018-03134-x

Zhao, J., Bower, A., Yang, J., Lin, X., & Zhou, C. (2018).)Structure and formation of anticyclonic eddies in the Iceland basin. *Journal of Geophysical Research: Oceans*, *123*(8), 5341–5359. https://doi.org/10.1029/2018JC013886